Available online at www.sciencedirect.com
SCIENCE DIRECT
Journal of Non-Crystalline Solids 352 (2006) 255–272
JOURNAL OF NON-CRYSTALLINE SOLIDS
www.elsevier.com/locate/jnoncrysol

Morphology and microstructure in fused silica induced by high fluence ultraviolet 3ω (355 nm) laser pulses

Joe Wong *, J.L. Ferriera, E.F. Lindsey, D.L. Haupt, I.D. Hutcheon, J.H. Kinney

Lawrence Livermore National Laboratory, University of California, P.O. Box 808, Livermore, CA 94551, USA

Received 29 July 2005; received in revised form 11 November 2005

Abstract

The morphology and microstructure induced in high quality fused silica by UV (355 nm) laser pulses at high fluence (10–45 J/cm^2) have been investigated using a suite of microscopic and spectroscopic tools. The laser beam has a near-Gaussian profile with a $1/e^2$ diameter of ~0.98 mm at the sample plane and a pulse length FWHM (full width at half maximum) of 7.5 ns. The damage craters consist of a molten core region (thermal explosion), surrounded by a near concentric region of fractured material. The latter arises from propagation of lateral cracks induced by the laser-generated shock waves, which also compact the crater wall, ~10 μm thick and ~20% higher in density. The size of the damage crater varies with laser fluence, number of pulses, and laser irradiation history. In the compaction layer, there is no detectable change in the Si/O stoichiometry to within ±1.6% and no crystalline nano-particles of Si were observed. Micro- (1–10 μm) and nano- (20–200 nm) cracks are found, however. A lower valence Si^{3+} species on the top 2–3 nm of the compaction layer is evident from the Si 2p XPS. The results are used to construct a physical model of the damage crater and to gain critical insight into laser damage process.

PACS: 61.80.Ba; 61.72.Ji; 78.60.Hk; 76.30.Mi

Keywords: Radiation effects; Laser–matter interactions; Secondary ion mass spectroscopy; Defects; Photoinduced effects; Silica; Water in glass

1. Introduction

Because of its excellent optical transparency and uniformity in the UV (ultraviolet) region, high quality fused silica (SiO_2) is the material of choice for use in high-average and high-peak power laser systems [1–3]. Recent technological applications in telecommunication and far UV lithography for microelectronics [4] have led to considerable scientific interest in UV laser-induced morphological and microstructural modification (damage) in fused silica used for transparent optics [5–7]. Obscuration loss and near-field intensity modulation resulting from laser-induced damage on the optical surfaces largely determines the operational lifetime of SiO_2 components. The obscuration may conceptually arise from two processes: initiation of damage at an absorbing site at or near the exit surface, and damage growth upon subsequent irradiation [8,9].

To establish a knowledge-based methodology to mitigate or obviate laser-induced damage growth at the exit surface [10], it is beneficial to elucidate the mechanism associated with the damage process and to identify the damage initiators. Critical to this process is the knowledge of various microstructural and morphological features of the damage sites created under various laser parameters and environmental conditions. The goal is to seek technically viable solutions to prolong the lifetime of optical components by reducing susceptibilities to laser-induced catastrophic breakdown.

This paper reports a systematic microscopic and spectroscopic study to elucidate in detail the morphology and microstructure over a large length scale from nm to mm

* Corresponding author. Tel.: +1 925 423 6385; fax: +1 925 423 4737.
E-mail address: wong10@llnl.gov (J. Wong).

0022-3093/$ - see front matter © 2005 Elsevier B.V. All rights reserved.
doi:10.1016/j.jnoncrysol.2005.11.036

of the damage craters induced on high quality fused silica by high fluence UV 3ω (355 mm) laser pulses. The data are used to construct a realistic model of the damage site and to acquire physical insight into the laser damage process.

2. Experimental

2.1. Samples and damage generation

The fused silica substrates were 50 mm diameter by 10 mm thick, and optically polished on both surfaces. The fused silica was manufactured by flame hydrolysis and contained 800–1000 ppm by weight of OH (Corning 7980) [11]. Low conductivity water was first used to rinse off any particles on the optic surface due to storage and handling. This was followed sequentially by a soap cleaning with a surfactant, rinsing the soap off with de-ionized water and a final alcohol rinse with absolute (200 proof) ethanol to remove residual water. The optics were then air dried in a laminar hood prior to irradiation with the 3ω laser pulses.

Laser damage sites were created at ambient conditions using a 3ω, 355 nm beam from a frequency tripled Spectra Physics GCR Nd-YAG laser with pulse length FWHM (full width at half maximum) of 7.5 ns and laser repetition rate of 10 Hz [12]. The beam profile was near-Gaussian with a $1/e^2$ diameter of $\sim$0.98 mm at the sample plane. Damage sites were produced exclusively on the laser exit surface [10] using single or multiple pulses with fluences ranging from 10 to 45 J/cm^2. The energy of each pulse was measured using a calorimeter. A second beam pickoff was directed to a CCD beam profiling system which images the beam in an equivalent plane to the sample and determines the peak fluence upon calibration with the energy. The layout of the laser system and associated optics is shown schematically in Fig. 1. Details of the components and system operation have been described elsewhere [12].

2.2. SEM

The microscope was a Hitachi S-4500, cold cathode, field emission scanning electron microscope (SEM). The specimen chamber was operated at a vacuum level of 7×10^{-4} Pa. The specimens were lightly coated with $\sim$200 Å of carbon, and imaged at acceleration voltages ranging from 1.5 to 10.0 kV and probe current $\sim$200 pA. Imaging was done primarily with secondary electrons using an Everhart-Thornley electron detector. The SEM Images were captured digitally with Quartz PCI digital imaging system controlled by a PC computer.

2.3. White light interferometry

A WYKO NT-2000 interferometer was used to record the depth profiles of the damaged craters by combining the light reflected off the sample surface and an internal reference surface to produce interference fringes when the sample is aligned and in focus. In the vertical scanning interferometry (VSI) mode used in this work, the surface was profiled by scanning the interferometric objective vertically downward so that each point on the surface produced an interference signal. A linearized piezoelectric transducer controlled the vertical motion. The white-light beam used in VSI mode had a short coherence length and interference fringes were present only over a very shallow depth for each focus position. At equally spaced intervals during the scan, frames of interference data imaged by the video camera were captured and processed. The system located the peak of the interference signal for each point on the surface and processed them in parallel to determine the surface height profile.

The detector used was a 736×480 pixel CCD. The lateral resolution was a function of the detector size and objective magnification. At an objective magnification of 50.1×, the lateral resolution is 0.18 μm/pixel for an actual areal map of 120 μm × 90 μm. For depth measurement,

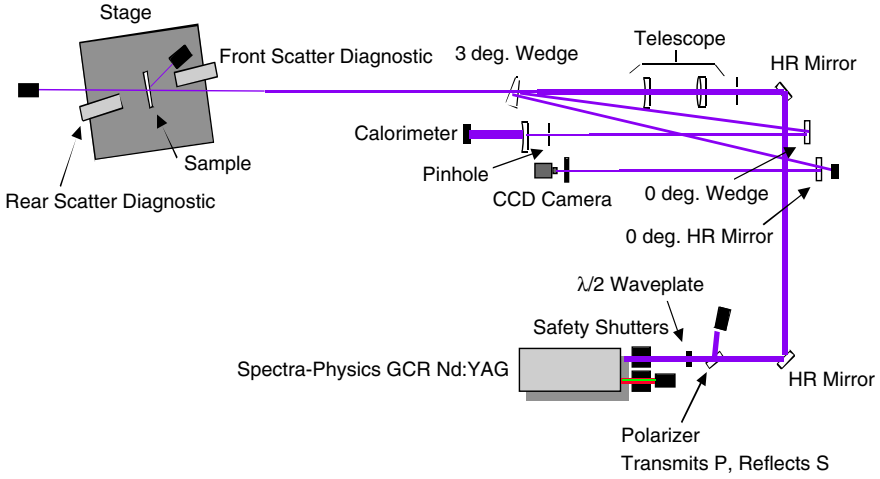

Fig. 1. Schematic layout of the 3ω laser system and associated optics used in this study, after Sheehan et al. [12].

the vertical resolution is 3 nm RMS for a flat surface. Vertical and lateral accuracy was checked periodically with calibration standards.

2.4. Phase shift interferometry

A phase shift Fizeau interferometer (Zygo, model MarkIV XP) was used to measure surface topography of the 3ω damage sites in fused silica. The device utilizes a low-power, circularly polarized helium–neon laser as a light source. The laser beam is de-magnified to a 4-inch diameter, collimated and exits the system through the aperture. A transmission element mounted in front of the aperture reflects some of the laser light back into the interferometer creating a reference wave front. The remainder of the light is transmitted through and illuminates the sample and is then returned to the interferometer and interferes with the reference wave front. The phase differences between these wave fronts result in an image of light and dark band (fringes). This image is converted into an electrical signal by a CID (charge injection device) camera with a $260(H) \times 210(V)$ resolution.

A piezoelectric crystal was used to precisely move the transmission element back and forth, causing the constant phase variations between the two wave fronts. During data acquisition the camera recorded measurements at each point when the interfering wave fronts underwent a 90-degree phase shift in relation to one another. These were then processed by a PC to determine the phase at each point of interference resulting in an accurate map of the wave front of the sample under test.

2.5. XMT

The XMT (X-ray microtomography) experiments were conducted on the 31-pole wiggler beam line, BL 10-2 [13] at the Stanford Synchrotron Radiation Laboratory with SPEAR (Stanford Positron–Electron Accumulation Ring) operating at an electron energy of 3 GeV and an injection current of ~100 mA. The synchrotron white beam

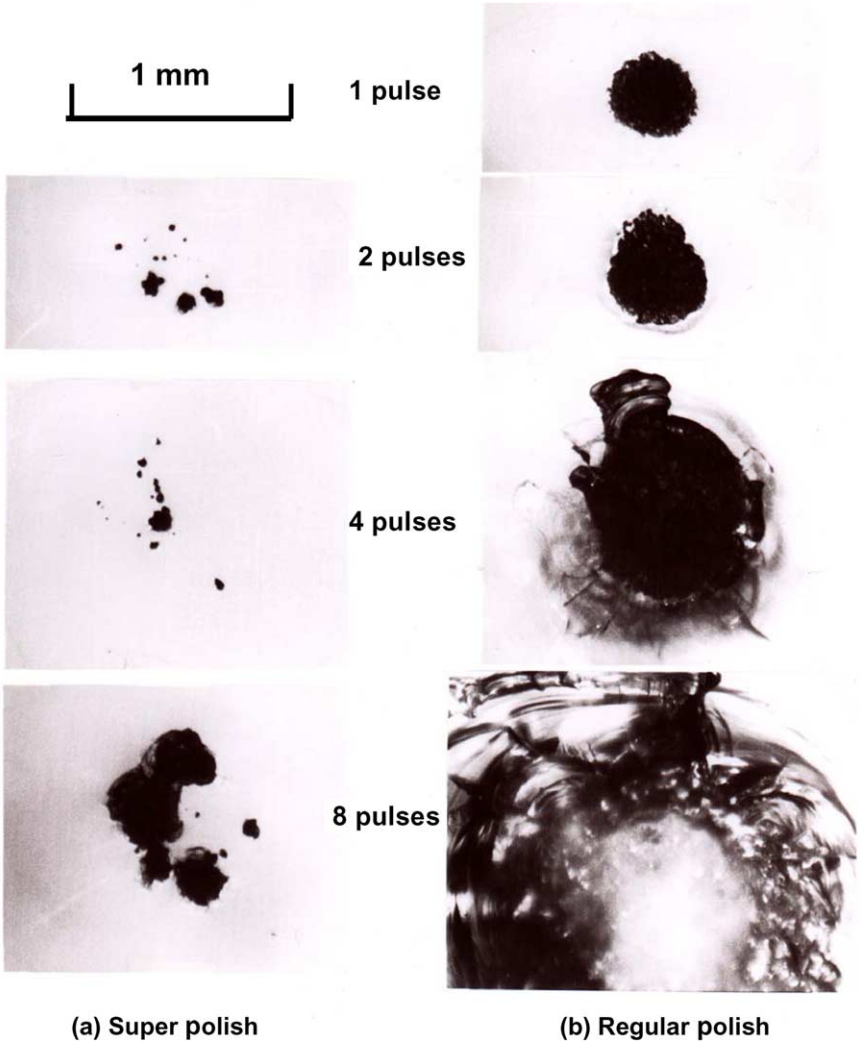

Fig. 2. Nomarsky optical micrographs of damage sites on fused silica surfaces (exit) as a function of number of 3ω laser pulses for (a) super polish surface and (b) regular polish surface. The laser parameters are: fluence = 35 J/cm^2, $1/e^2 = 0.98$ mm, pulse length (FWHM) = 7.5 ns and repetition rate = 10 Hz.

emerging from the 31 pole wiggler was monochromatized downstream with an asymmetric double-crystal Si(220) monochromator. The photon energy selected, 17 keV, was chosen to make the specimen diameter, 2.5 mm, equivalent to two absorption path lengths as this gives the best balance of contrast and resolution for most tomographic imaging. The XMT samples were cored ultrasonically from fused silica disks, 50 mm diameter × 10 mm thick, to form rods, 2.5 mm diameter × 10 mm high, prior to 3ω laser irradiation. The laser entrance and exit surfaces were protected with wax during coring.

The XMT apparatus [14] consisted of three translational stages used for overall specimen positioning and a fourth precision rotary stage for executing the angular increments. Two-dimensional radiographic images of the specimens were collected on a Photometrics CH350 camera having 9 μm pixels. Optical magnification of 5.4× and re-binning of the camera 2 × 2 was applied to give a net resolution of 3.33 μm per pixel. The camera records 12 bits of information per pixel or 4096 levels of intensity. The CH350 camera had a chilled detector running at −35 °C and has a very low dark current noise level. An angular increment of 0.25° was used.

Each scan began with an initial dark (background) reading, which was subtracted from each subsequent image. Then, at regular intervals of 7.5° beginning at 0°, reference images were taken with the sample moved out of the beam so that just the details of the beam itself are recorded. Care was taken that the exposure time did not lead to saturation of any bin in the camera. Generally, the maximum count was kept just below 4000. The reference images were used for the important purpose of normalizing all the specimen images to produce corrected radiographs in which no features attributable to the beam were present.

For a given XMT specimen, each of the 1440 radiographic images was transformed into a sinogram. The sinograms were used as input to the tomographic reconstruction algorithm utilizing a Fourier filtered back projection method and converted the data into the form of a 3D volume set of X-ray absorption values. A computer graphic package such as the IDL (Interactive Data Language, Kodak) cuts it on any plane or surface and displays a tomographic image of the specimen in a 'false' color scheme. Details of the image reconstruction and tomographic rendering have been described elsewhere [14].

2.6. HRTEM

High resolution and bright field TEM images were recorded using an FEI CM300FEG scanning transmission electron microscope operated at 300 keV. The point to point resolution is 1.9 Å with an image information limit of 1.2 Å. The microscope is also equipped with a Gatan GIF2000 image filtering system for chemical mapping and an Oxford SiLi detector with an Emispec digital acquisition system for energy dispersive analysis.

2.7. XPS

XPS spectra for Si were acquired on a Physical electronics Quantum 2000 ESCA system. The X-ray source was a monochromatic AlK_α (1486.7 eV) beam which was toroidally focused before collominated to a spot size of ~10 μm. The acceptance angle was ±23° to yield an analysis area of 50 μm. Prior to XPS measurements, the silica surface was first sputter-cleaned for 216 s with a 500 eV Ar^+ beam, rastering an area of 4 × 4 mm^2. This process removed 7–8 Å top contamination layer (mostly carboneous material). The energy resolution of the spectrometer was ±0.25 eV.

2.8. Microprobe analysis

Microprobe analyses for the Si/O stoichiometry in the damaged area were performed using a JEOL 733 Superprobe electron microprobe operated with a 10 keV, 5 nA electron beam, focused into a ~0.1 μm diameter spot. Due to indications of beam damage, two traverses were performed with modified protocols; these traverses are discussed in the next section. Quantitative analyses of O and Si contents were carried out by wavelength dispersive X-ray spectrometry. A polished, undamaged fused silica

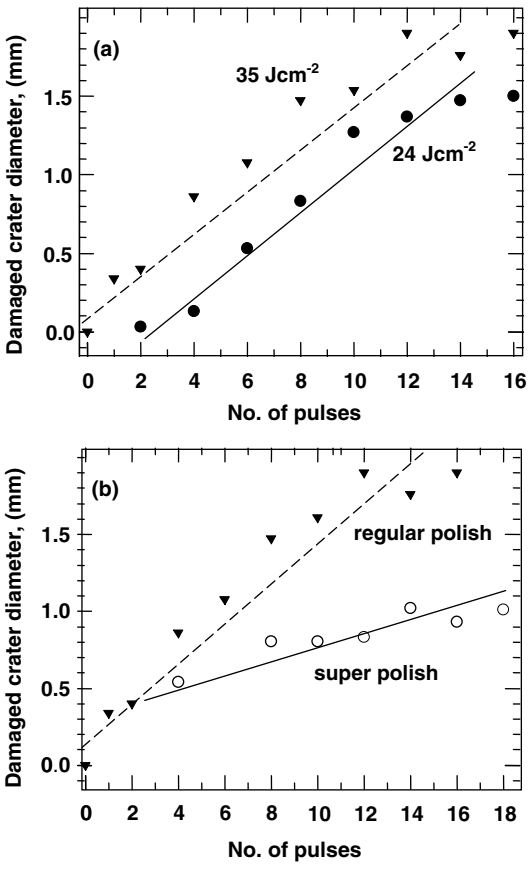

Fig. 3. Diameter of damage crater as a function of number of 3ω pulses (a) at laser fluences of 24 and 35 J/cm^2 on a regular polish surface, and (b) for regular and super polish surfaces at 35 J/cm^2. The lines are drawn as visual aid only. All other laser parameters are: $1/e^2 = 0.98$ mm, pulse length (FWHM) = 7.5 ns and repetition rate = 10 Hz.

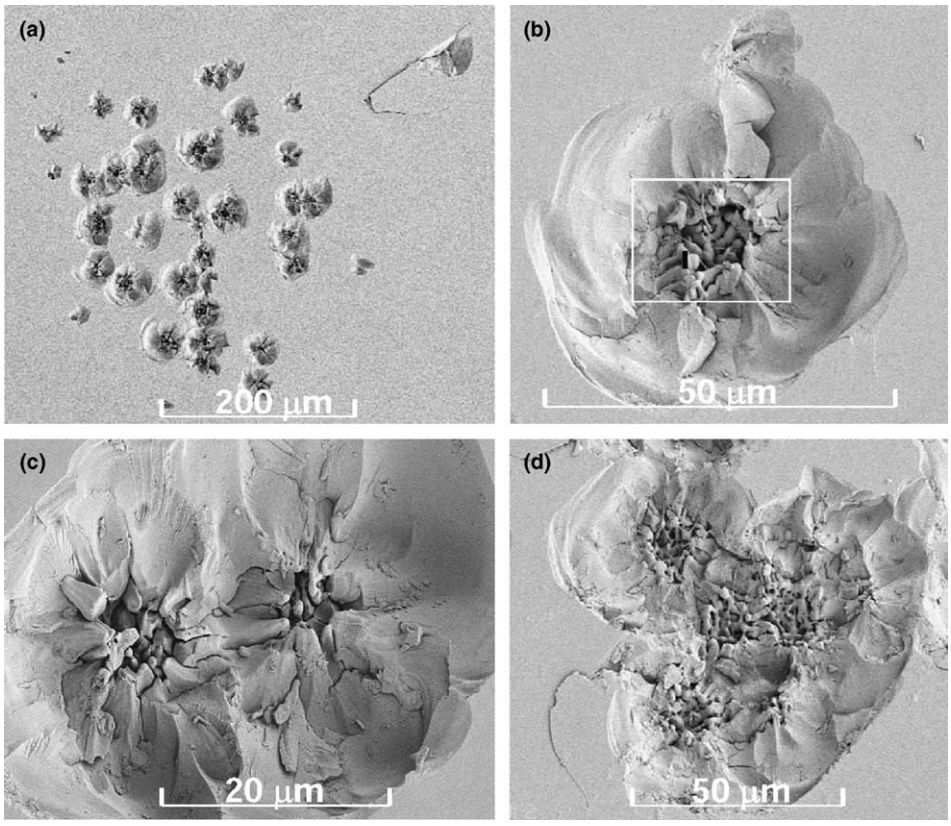

Fig. 4. (a) SEM micrograph of a damage region on a fused silica surface induced by a pulse of 3ω light at 45 J/cm^2, showing a cluster of pits and craters within the $1/e^2$ beam diameter (0.98 mm) on sample. The craters may be isolated (b), or as doublet (c), or multiplet (d). All other laser parameters are: pulse length (FWHM) = 7.5 ns and repetition rate = 10 Hz.

glass was used as the primary standard for both O and Si; natural quartz (SiO_2) was used as a secondary standard. These standards were carbon-coated at the same time as the damaged optic to avoid any systematic errors associated with differential absorption of low energy O K_α X-rays in the carbon-coat. X-ray intensities were converted to element concentrations using a commercial CIT-ZAF algorithm.

2.9. SIMS analysis

The hydrogen content in the damaged sites was analyzed with a modified Cameca ims-3f ion microprobe. A 1 nA $^{16}O^-$ primary ion beam focused into a ~3 μm diameter spot was rastered over a 12×12 μm^2 area of the sample at each point of analysis. An aperture inserted in the sample image plane allowed only positive secondary ions arising from a 4 μm diameter circular region in the center of the rastered area, and with a nominal energy of 4500 eV, to enter the mass spectrometer. Analyses were performed in a step-scan mode. Each traverse began at least 50 μm from the sample edge and proceeded toward the contact with the epoxy and Si marker (see Fig. 18 later). Each position along a traverse was analyzed with the following protocol. The area was pre-cleaned by rastering the primary beam for ~5 min. Once the H^+/Si^+ ratio had stabilized, indicating removal of surficial H, the data collection was begun and 3–5 blocks of 10 cycles each were collected. Each cycle comprised the mass sequence 0.95, ^1H, ^{30}Si. Following the end of each analysis, the stage was moved to the next position and the sequence was repeated. To reduce the background from adsorbed water vapor, the sample was loaded 24 h prior to commencement of analyses and was surrounded by an annular plate cooled with liquid nitrogen. The pressure in the sample chamber during the analysis was $\sim 2 \times 10^{-9}$ mbar.

3. Results

3.1. Overall size of damage craters

The size and morphology of 3ω damage sites in a silica are strongly dependent on the laser fluence, number of pulses and nature of the optic surface, e.g.: regular polish vs super polish [15]. Fig. 2 shows a series of Nomarsky optical micrographs of damage sites, each irradiated with a 3ω beam at 35 J/cm^2 as a function of number of pulses for (a) a super polish surface (RMS surface roughness ~0.1 Å) and (b) a regular polish surface (RMS surface roughness ~0.5 Å). Qualitatively, the super polish surface is more resistant to damage in terms of fluence threshold and areal extent of the damage site. Quantitatively, the diameter of the damage crater increases monotonically with the number of pulses and is also a function of the laser fluence as shown

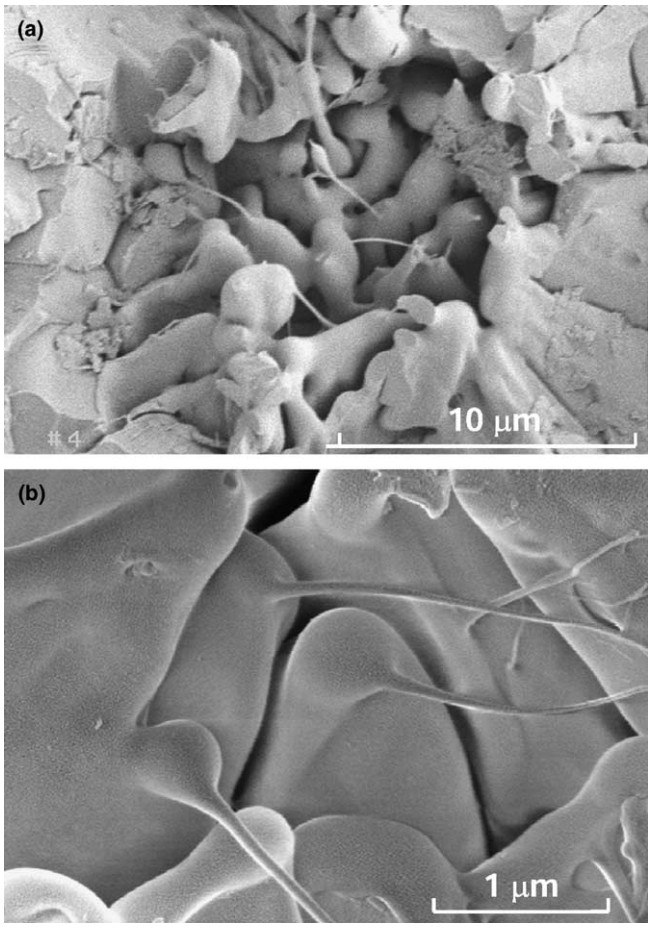

Fig. 5. High magnification SEM micrographs of the center region of the damage crater shown in Fig. 4(b) showing (a) a molten and (b) fibrous morphology, evident of a thermal explosion at the core region of the crater.

in Fig. 3(a). The damage growth rate is also a function of the nature of the silica surface as shown in Fig. 3(b) for super polish vs regular polish.

3.2. Morphology of damage craters

The morphology of damage regions in fused silica resulted from irradiation of a pulse of high fluence 3ω light consists of a collection of erosion pits (craters) spanning a fraction of the $1/e^2$ beam size on sample. Fig. 4(a) shows such a damage morphology induced by a pulse of 45 J/cm^2 3ω light with a temporal pulse width of 7.6 ns and a $1/e^2$ beam diameter of 0.98 mm on sample. The craters may be isolated as shown in Fig. 4(b), or a doublet shown in Fig. 4(c), or as a cluster of multiple craters shown in Fig. 4(d). SEM examinations at higher magnification revealed that these damage craters consist of a core of molten nodules with a botryoidal morphology (Fig. 5(a)) and fibers (Fig. 5(b)) evident of a thermal explosion followed by quenching from the liquid state at this high-energy absorption region. The molten core is surrounded concentrically by an annulus of fractured material, indicative of mechanical damage accompanied by spallation of material as evident in Fig. 4(b). At yet a higher magnification, micron and sub-micron digs, pits and surface cracks are also identified. These sub-micron features are shown in Fig. 6. No molten core was evident in these pits, but instead fractured debris was found as shown in Fig. 6(d).

The depth morphology of the craters shown in Fig. 4(a) was determined using stereographic SEM imaging. The depth profile along a selected cross section may be obtained quantitatively by simple geometry using

$$z = P/[2M(\sin\alpha/2)], \quad (1)$$

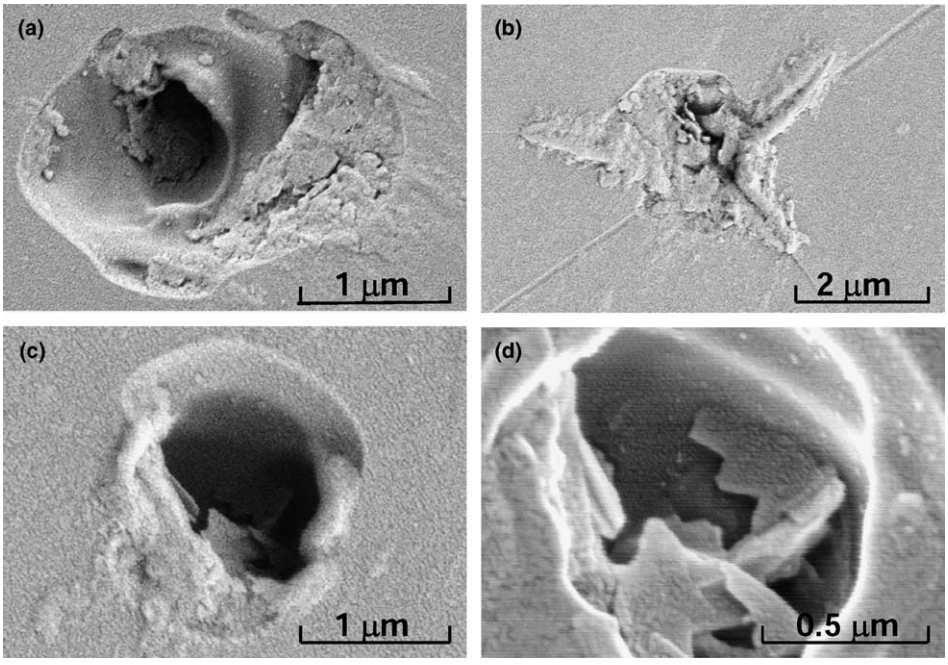

Fig. 6. SEM micrographs at higher magnification showing sub-micron digs, pits and surface cracks in the same irradiated region shown in Fig. 4(a).

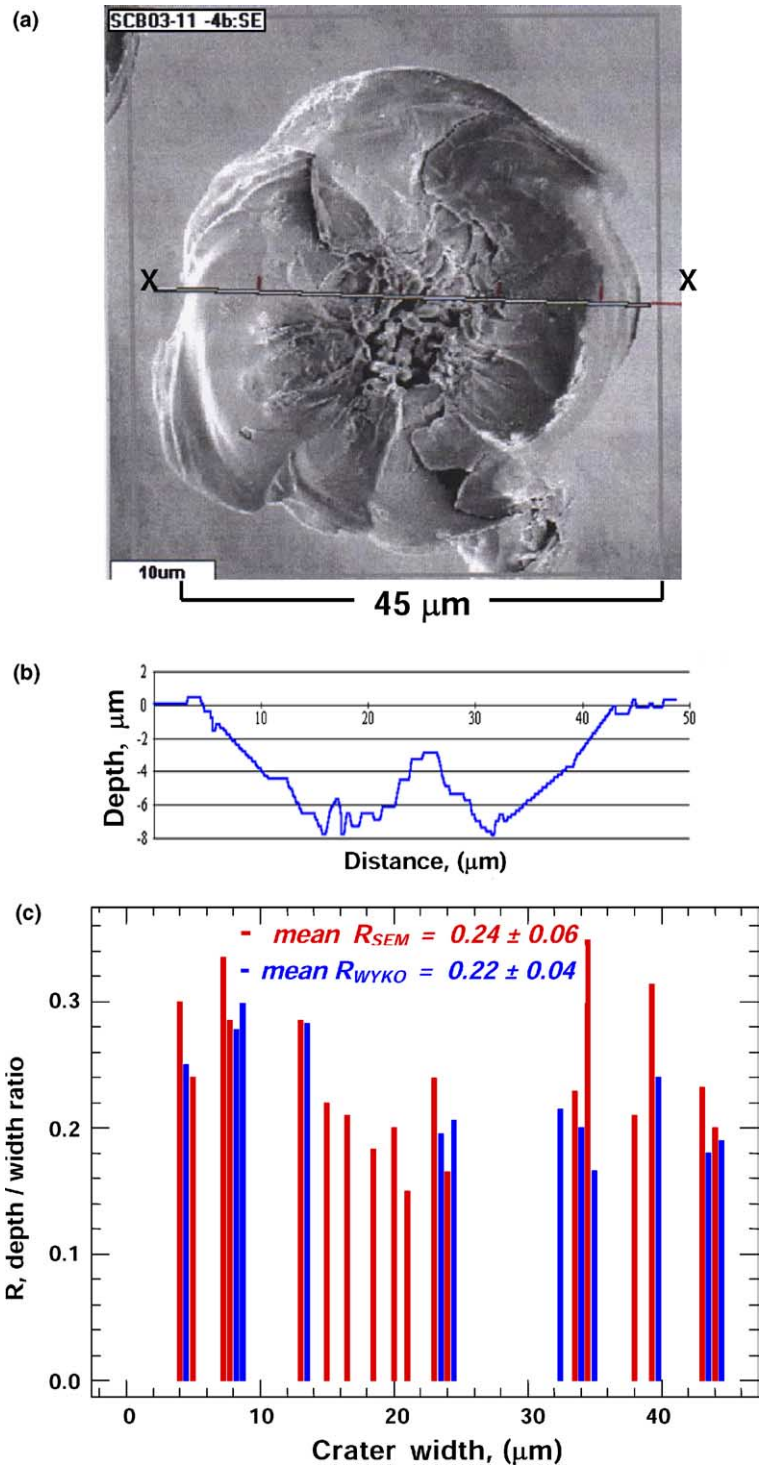

Fig. 7. Depth profiling of damage crater: (a) stereo-SEM stereo micrograph of same crater shown in Fig. 4(a) and (b) corresponding depth profile of a vertical section X–X, and (c) plot of the aspect ratio of depth to diameter as a function of crater diameter using stereo SEM and white light interferometry.

where z is the depth, P is the parallax, M is the magnification of the SEM measurement and α is the tilt angle between the stereo pair of images [16]. The results are illustrated in Fig. 7. The damage crater shown in Fig. 4(b) is reproduced as a stereo SEM micrograph in Fig. 7(a) [17]. The depth profile along a vertical cut X–X computed using the above equation is also shown in Fig. 7(b). By repeating the same procedure for all the isolated craters shown in Fig. 4(a), the width and depth of some 20 isolated crater were determined. The results are given in Table 1 from which an average aspect ratio of depth to width was determined to be 0.24 ± 0.06. The results are plotted in Fig. 7(c) as the red histogram.

Table 1
Aspect ratio of depth to diameter (z/d) of damage crater in fused silica induced by 3ω irradiation determined by stereo SEM and WYKO white light interferometry

Crater	d_{SEM}	z_{SEM}	z/d (SEM)	d_{WYKO}	z_{WYKO}	z/d_{WYKO}
1	4	1.2	0.3	1	4	0.25
2	5	1.2	0.24	–	–	
3	7.4	3.18	0.335	2.06	7.4	0.28
4	7.7	3.15	0.285	2	6	0.3
5	13	3.7	0.285	5.95	21	0.283
6	15	3.3	0.22	–	–	–
7	18.5	3.4	0.183	–	–	–
8	16.5	3.6	0.21	–	–	–
9	20	4	0.20	–	–	–
10	20	3	0.15	–	–	–
11	23	10.1	0.239	4.5	23	0.195
12	23	3.8	0.165	8.25	40	0.206
13	32	–	–	6.9	32	0.215
14	33.5	9.65	0.229	6	30	0.20
15	33.5	11.58	0.345	5	30	0.166
16	38	8.12	0.21	–	–	–
17	39.3	12.37	0.314	7.3	30	0.24
18	43	9.58	0.232	9.4	45	0.18
19	44	9.68	0.22	7.9	41	0.192
	Mean: 0.24(3) ± 0.05(8)			Mean: 0.22(5) ± 0.04(4)		

The craters enumerated are shown in Fig. 4(a). All dimensions in μm.

The stereographic SEM depth profile measurements were calibrated with white light interferometry using a WYKO NT-2000 microscope operating in a VSI mode. A typical areal interferogram is shown in Fig. 8, the crater

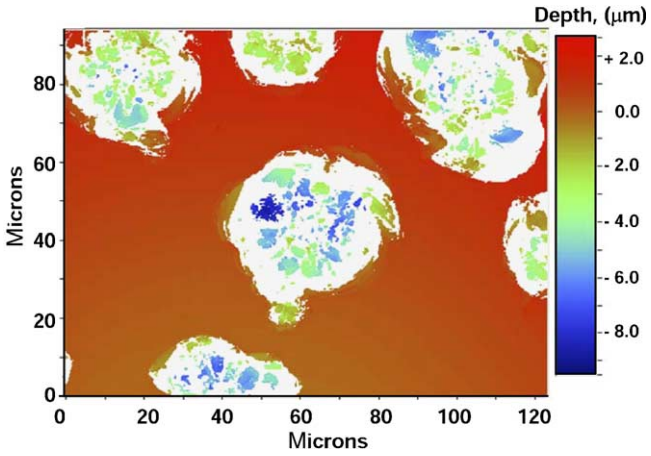

Fig. 8. White light interferogram and depth profile of an area in the vicinity of the 3ω damage crater in fused silica shown in Fig. 4(a) using a WYKO interferometer. The WYKO data are used to calibrate the depth profile from the SEM anaglyphs like that shown in Fig. 7(a).

in the center of which corresponds to the same crater shown in Fig. 4(b) and Fig. 7(a). The interferometric results are also given in Table 1, and plotted in Fig. 7(c) as the blue histogram which yields an average value for the aspect ratio of 0.22 ± 0.04. This corroborates well with the stereo-SEM result. Interestingly, this ratio is similar to an aspect ratio of ~0.20 observed and calculated for craters created by both meteor impact as well as underground explosion [18–20].

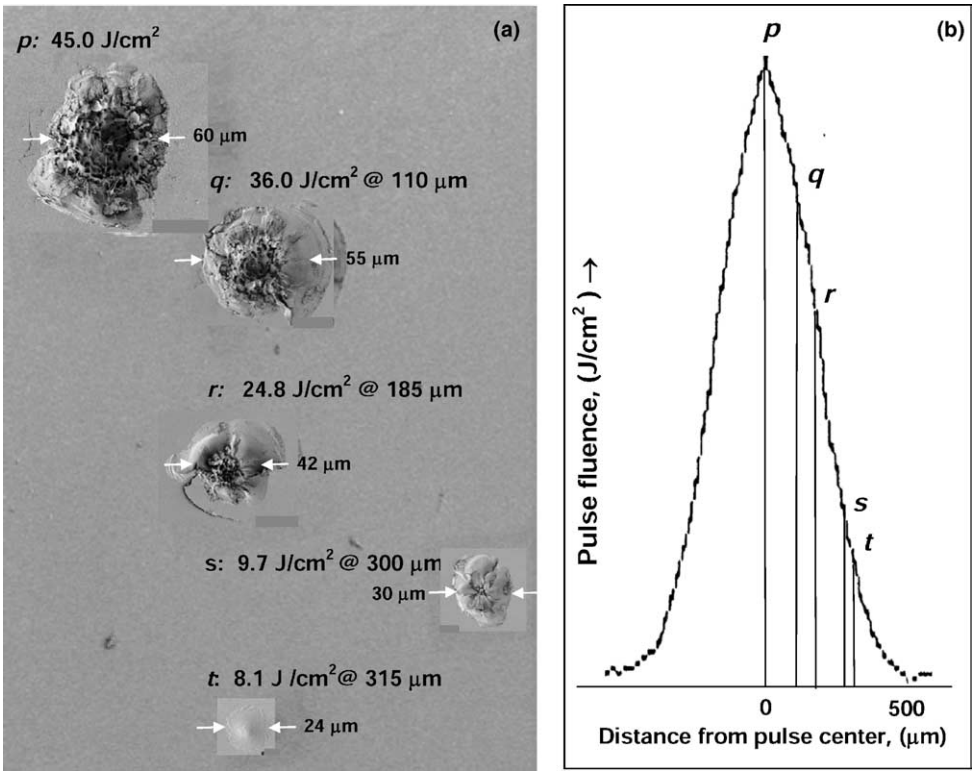

Fig. 9. (a) Crater size variation along a fluence gradient on sample as shown in (b) at p, q, r, s and t within the same 3ω laser pulse having a peak fluence of 45 J/cm^2. All other laser parameters are: $1/e^2 = 0.98$ mm, pulse length (FWHM) = 7.5 ns and repetition rate = 10 Hz.

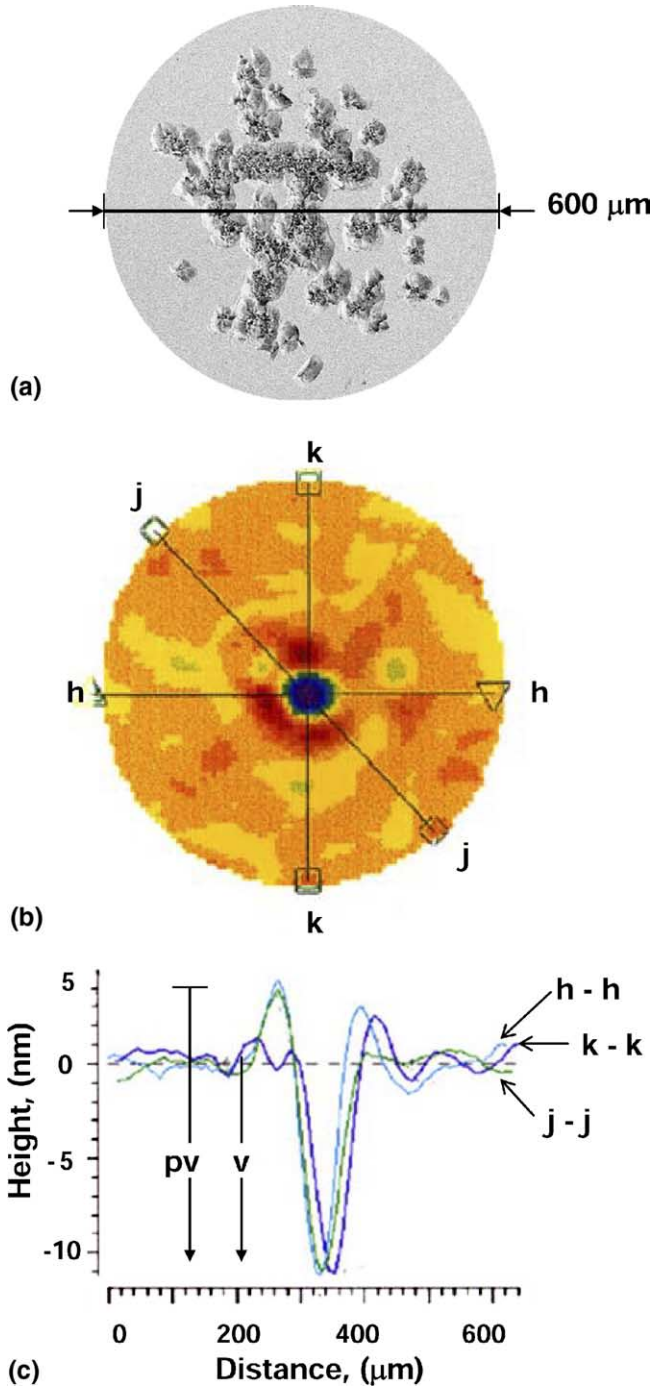

Fig. 10. Surface topography of the same damage site induced in fused silica by a pulse of 3ω laser at 45 J/cm^2 similar to the one shown in Fig. 4(a). (a) SEM micrograph of the damage site, (b) laser-shift interferogram of the site covering a 600 μm diameter and (c) topographic profiles of three representative vertical traverses. The zero of the height level in (c) is that of the surface RMS value as described in the text.

It is interesting to note that the Gaussian profile of the 3ω beam having a $1/e^2$ beam diameter of 0.98 mm (980 μm) at the sample plane produces a radial fluence gradient on the irradiated silica glass. This in turn would give rise to variation of crater size and morphology on the silica glass. Such morphology variation is illustrated in Fig. 9(a)

Table 2
Surface topography of damage craters determined by laser phase shift interferometry

Crater	RMS surface	pv	v	pv–v	Rim diameter (μm)
1	1.2	16	11	5	133
2	2.4	30	22	8	162
3	1.8	26	20	6	130
4	2.4	20	15	5	125
Mean	1.9 ± 0.6	23 ± 6	17 ± 5	6 ± 1.4	137 ± 16

Dimensions for RMS surface, pv (pile-up peak to valley), v (surface to valley) and pv–v are in nm. See Fig. 10(c).

which shows a series of SEM images of damage craters along the fluence gradient on sample. Fig. 9(b) is the measured beam profile having a peak value of 45 J/cm^2. From this profile and the distances from the SEM micrograph (Fig. 9(a)) of the various craters at q, r, s and t from the main crater at p, which was presumably created at the beam peak fluence, a local fluence of 36, 24.8, 9.7 and 8.1 J/cm^2 can be deduced at the respective sites. As evident in Fig. 9(a), the size and overall morphology of the crater vary with the beam fluence at location. More interestingly, the '*molten core + fracture annulus*' morphology is retained

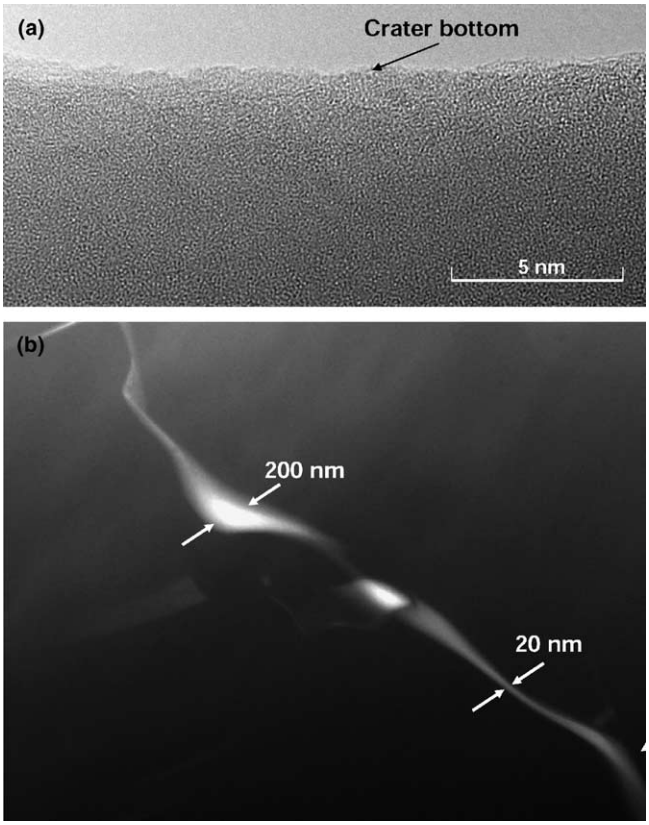

Fig. 11. (a) HRTEM micrograph of the bottom of a damage crater induced in fused silica by 2 pulses of 3ω light at 35 J/cm^2, revealing an amorphous structure and absence of crystalline nano-particles to a depth of ~10 nm, and (b) nano-size cracks below the crater bottom. All other laser parameters are: $1/e^2 = 0.98$ mm, pulse length (FWHM) = 7.5 ns and repetition rate = 10 Hz.

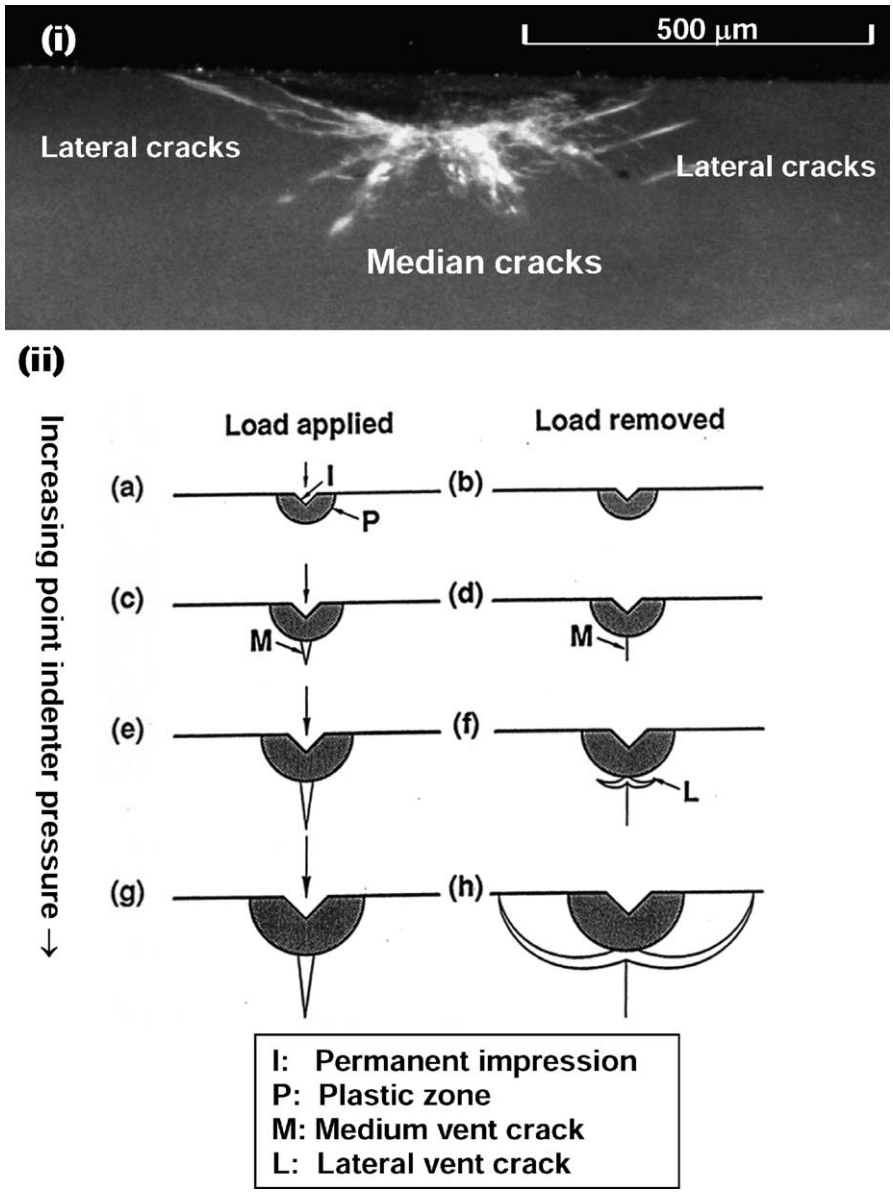

Fig. 12. (i) Cross sectional optical micrograph of a damage crater induced in fused silica by 6 pulses of 3ω light at 24 J/cm^2 showing the crack morphology. All other laser parameters are: $1/e^2 = 0.98$ mm, pulse length (FWHM) = 7.5 ns and repetition rate = 10 Hz. (ii) Schematics of plastic deformation to brittle fracture transition in a glassy material with increasing load and resultant crack morphology upon load removal (after Lawn and Swain [23]).

down to a fluence of ~10 J/cm^2. Below this fluence, no molten core is evident and the morphology of the damage site is not as dramatic.

3.3. Surface depression and rim pile-up

The surface topography of the damage sites was examined using laser phase shift interferometry. The results for a typical damage site are given in Fig. 10. Fig. 10(b) is an interferogram of a damage site created with one pulse of 3ω light at 45 J/cm^2. Various representative depth profiles, r–r, p–p and s–s across a 600 μm diameter of the damage site (Fig. 10(c)) indicate that there is a general surface depression of ~10 nm with respect to the surface RMS value. In addition, these profiles also show that there is a 4–5 nm pile-up at a rim with a diameter of ~140 μm. Topographic data for four similar damage sites were collected and summarized in Table 2. These results rendered an average surface depression of 17 ± 5 nm, and a pile-up of 6 ± 1.4 nm with an average rim diameter of 137 ± 16 μm.

3.4. Cracks

HRTEM was employed to search for nano-particles and nano-cracks in the 3ω damaged silica. Fig. 11(a) is a HRTEM micrograph of a representative location at the bottom of the damage crater created by 2 pulses of 3ω light at 35 J/cm^2 having the usual laser parameters. The micro-

graph is typical of an amorphous solid and no nano-crystalline particles are evident due to the absence of any regular lattice domains characteristic of crystalline materials [21,22]. However, nano-cracks varying from 10 to 200 nm wide are observed at regions in the bulk material well below the bottom of the crater as shown in Fig. 11(b). These nano-cracks can grow into micro-cracks (microns in width) with increased number of pulses (damage growth) and become observable with optical microscopy. Fig. 12(i) is a cross sectional optical micrograph showing the crack pattern beneath a damage crater created with 6 pulses of 3ω light at 24 J/cm^2. Median cracks at the bottom of the damage crater and lateral cracks flanking on both sides are evident. Such a pattern conforms qualitatively to those discussed by Lawn and Swain [23] for a plastically deformed material under a permanent impression at increasing load as shown schematically in Fig. 12(ii).

4. Discussion

4.1. Compaction layer

Fig. 13 displays a series of XMT cross sectional images of a 3ω damage crater on the laser exit surface of the fused silica rod. The crater was created at ambient conditions in air with 310 pulses of 3ω beam with a peak fluence of 12 J/

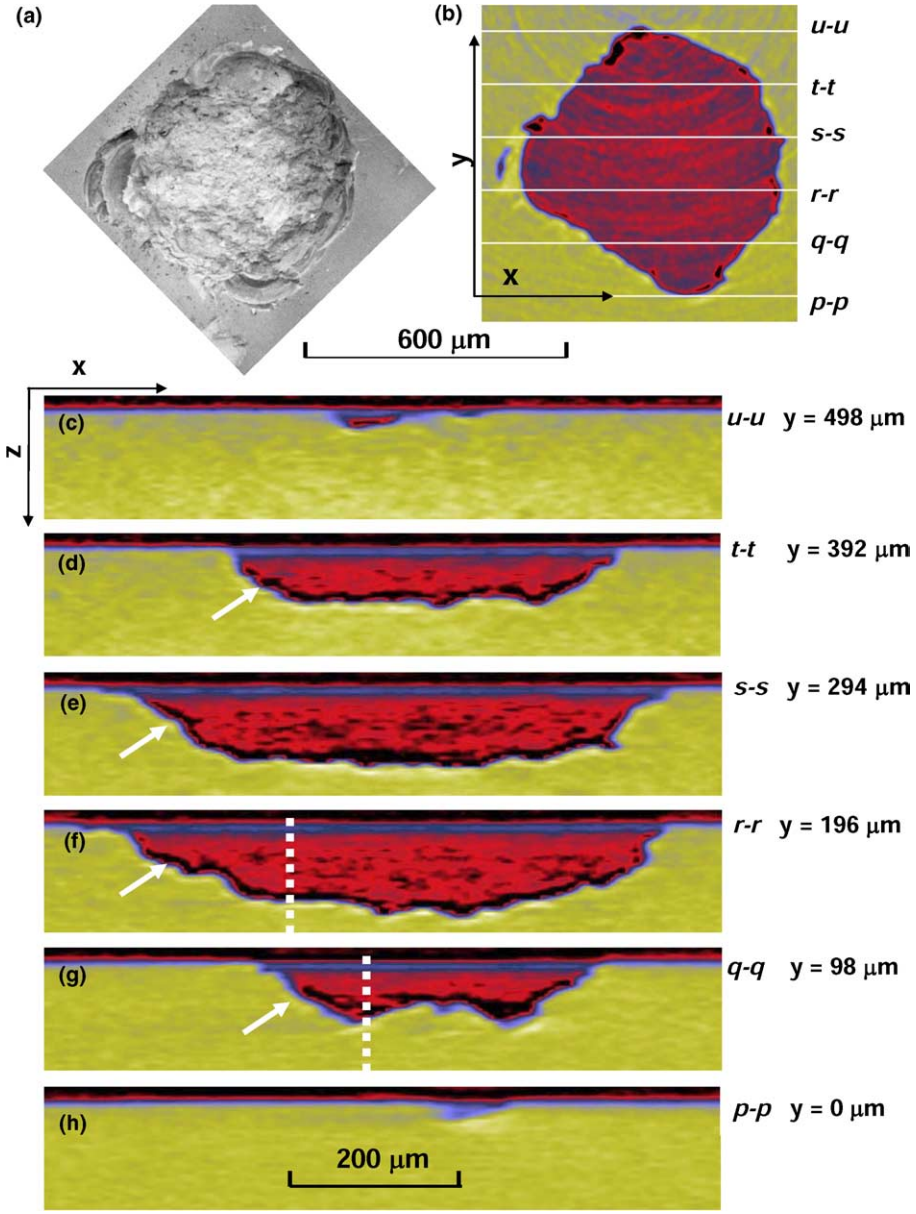

Fig. 13. (a) SEM micrograph, and (b)–(h) X-ray tomographic cross sections, of a damage crater in fused silica induced by 310 pulses of 3ω laser light at 12 J/cm^2. All other laser parameters are: $1/e^2 = 0.98$ mm, pulse length (FWHM) = 7.5 ns and repetition rate = 10 Hz. (a) and (b) are top views; (c)–(h) are vertical xz cross sections, each 3.3 μm thick at equal intervals at 98 μm along y. The white arrows in panels (d)–(g) indicate location of the compaction layer.

cm^2. Fig. 13(a) is a top-view SEM image of the damage site ~600 μm in diameter. The corresponding XMT image is shown in Fig. 13(b). Tomographic slices in the x–z plane, each 3.3 μm thick, and at an even y-spacing of 98 μm are shown in Fig. 13(c)–(h). Red color in the XMT image denotes void space in the damage crater and dark green denotes silica material. Careful inspection of the images reveals a bright (continuous) yellow fringe at the bottom and (somewhat discontinuous) at walls of the crater (white arrows in Fig. 13(d)–(g)).

High resolution electron microprobe analysis (next section) shows that the Si/O stoichiometry at the bottom of damage crater to a depth of 100 μm was invariant with that of an undamaged fused silica standard within experimental accuracy. Thus, at a given chemical composition, the X-ray absorption value of a material is a direct measure of its physical density as evident from Lambert law: $\mu = 1/t\log(I_o/I) = \mu_m\rho$, since X-ray attenuation in matter as determined by the linear absorption coefficient, μ, is a mass absorption effect, $\mu_m\rho$, where μ_m is the mass absorption coefficient of the given element or compound and ρ, its physical density. Line profiles at locations (dotted lines) indicated in Fig. 13(f) and (g) show a 20–22% overshot in absorption value above the constant bulk value at the bottom of the crater to a depth of ~10 μm. The absorption profiles (Fig. 14) were performed using a step size of 1.1 μm. A three-dimensional tomographic rendering of the whole compaction layer is given in Fig. 15, which indeed shows that it is rather continuous at the crater bottom, but somewhat discontinuous on the walls.

Similar XMT measurements and analyses have been performed on other 3ω damage craters in fused silica produced under different laser parameters. All yield a ~20% compaction layer and ~10 μm thick. For example, Fig. 16 show results for a damage site created by a single 3ω laser pulse at 35 J/cm^2, other laser parameters being the same. The damage site consists of a cluster of small craters clearly evident in the SEM micrograph (Fig. 16(e)). Top views of tomographic slices, each 3.3 μm thick and at a spacing of 5.5 μm in the z direction toward the bottom are shown in Fig. 16(b)–(d). Bright yellow fringes are again evident at the bottom of each individual crater as shown in Fig. 16(d). Fig. 16(a) is a tomographic cross section along p–p shown in Fig. 16(b). Fig. 16(f) shows an absorption profile along a v–v cut from the surface to the bottom of the one of the isolated crater, Fig. 16(e). The results again yield a compaction layer with ~20% densification and 10 μm thick as shown in Fig. 16(f).

Furthermore, it is of interest to correlate the current densification result with the equation of state of fused silica from shock measurements [24]. As can be seen in Fig. 17, fused silica is highly compressible to ~30 GPa. Assuming negligible density relaxation after the passage of the shock wave, it may be inferred that the compaction of fused silica by 3ω laser irradiation occurs at ~10 GPa (and higher pressure, if density relaxation took place). This is consistent with the gas-gun results of Sugiura et al. [25] that permanent densification in fused silica starts at ~8.8 GPa and completes at 16 GPa.

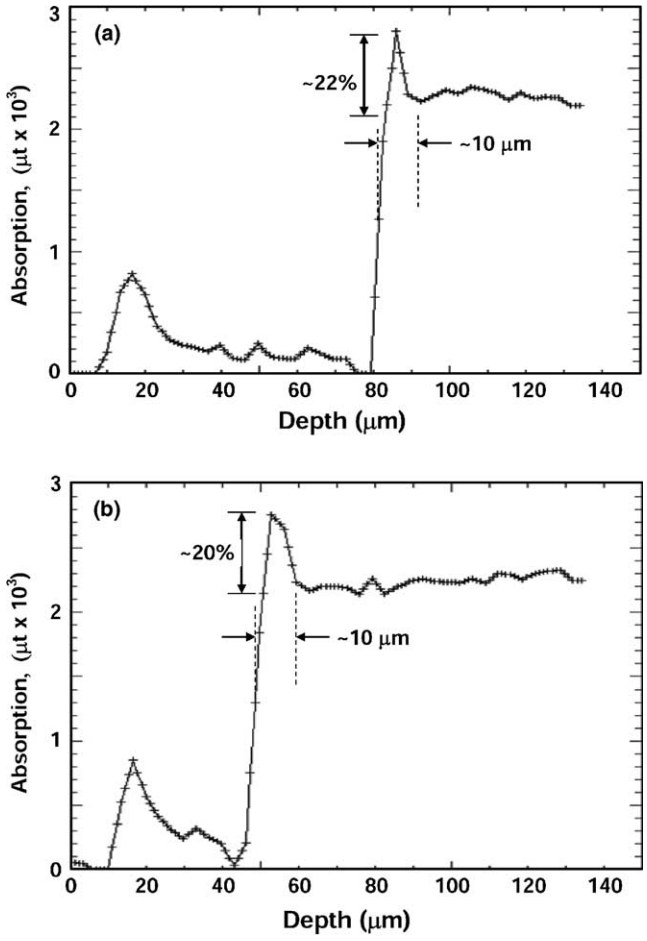

Fig. 14. X-ray absorption profiles showing a 20–22% compaction layer, ~10 μm thick at the bottom of the crater along the dotted lines shown (a) in Fig. 13(f), and (b) in Fig. 13(g).

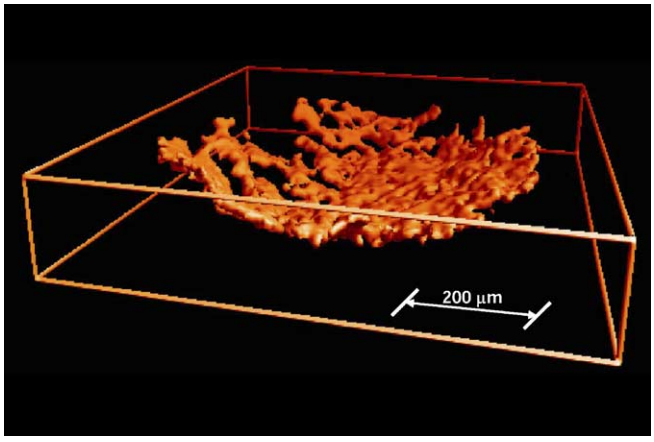

Fig. 15. A three-dimensional rendering of the compaction layer associated with the damage crater show in Fig. 13. The compaction layer is rather continuous at the bottom, but somewhat discontinuous at the walls.

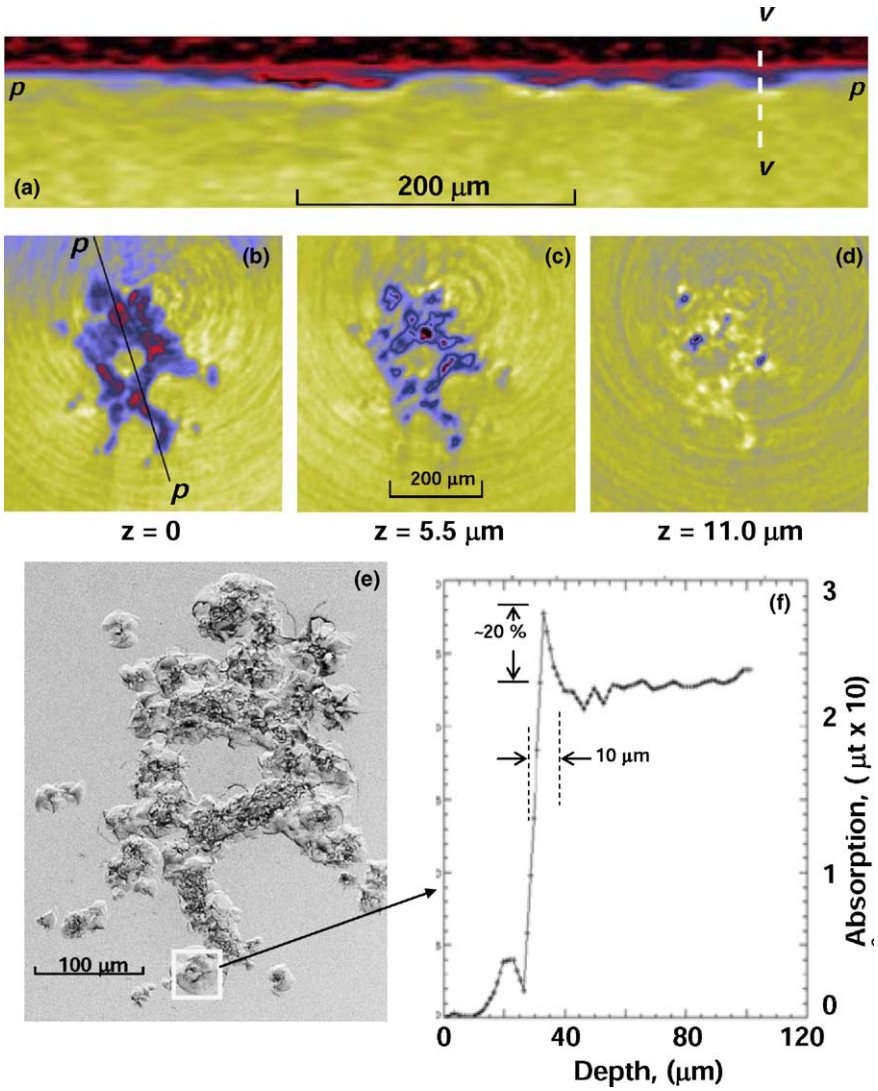

Fig. 16. (a)–(d) X-ray tomographic cross sections, each 3.3 μm thick, of a damage site induced by a pulse of 3ω laser light at 35 J/cm^2 in fused silica. All other laser parameters are: $1/e^2 = 0.98$ mm, pulse length (FWHM) = 7.5 ns and repetition rate = 10 Hz. (e) is an SEM micrograph (top view) and (f) an absorption line profile along v–v in (a) of an isolated crater shown in (e). Again, a ~20% compaction layer, ~10 μm thick is identified.

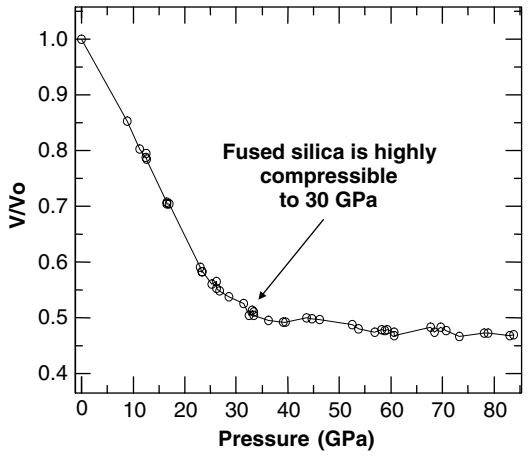

Fig. 17. Equation of state for fused silica at room temperature plotted as V/V_o vs pressure derived from shock measurements [24]. The line drawn through the data points serves as a guide to the eyes.

4.2. Si/O ratio, H in SiO_2 and low valence Si^{3+} species

4.2.1. Si/O stoichiometry

The Si/O stoichiometry in the region of the damaged crater has been determined with electron microprobe analysis. A damage crater, created with one pulse of 3ω beam at 35 J/cm^2 was used for the analysis. Seven traverses, each 100 μm in length, in locations corresponding to the map shown in Fig. 18(a) were probed: three traverses A, B, and E in the center of the damage crater, two traverses L and R on opposite sides, each roughly midway between the crater center and the crater rim and two traverses in an undamaged region, a few crater-diameters away from the crater (not shown in Fig. 18(a)). Initially, the spacing of the analyses along the traverses was adjusted to provide ~1–2 μm spatial resolution in the vicinity of the crater, increasing to 10 μm at distances exceeding 50 μm.

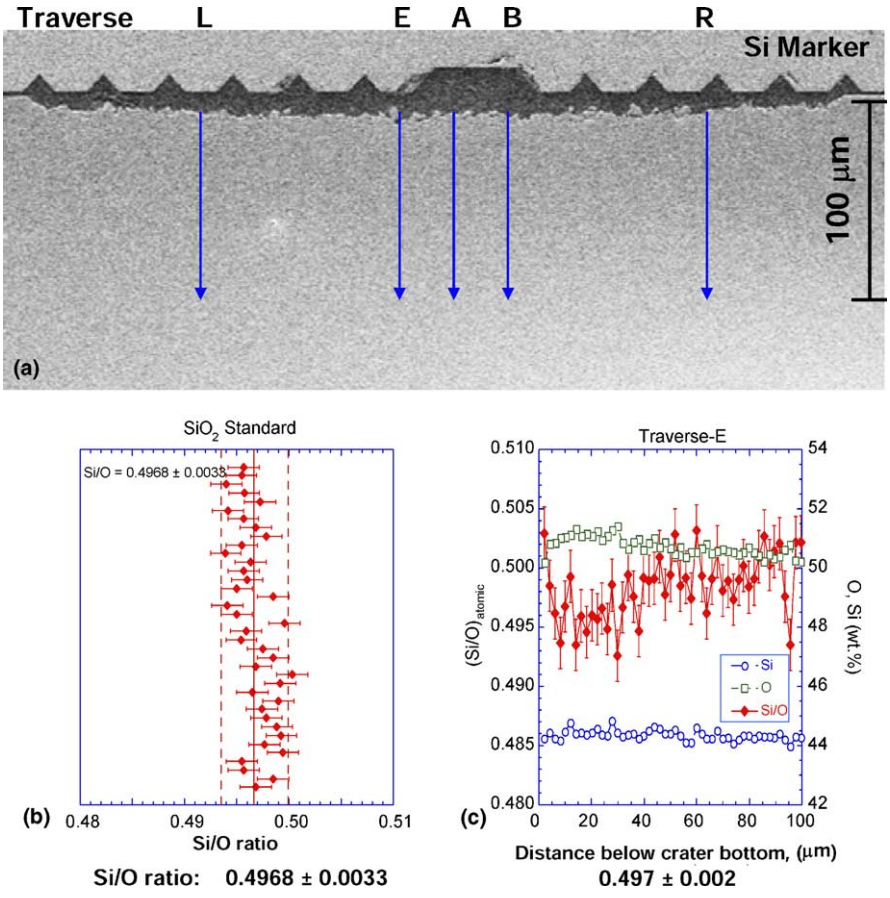

Fig. 18. (a) Cross sectional optical micrograph of a damage crater induced in fused silica by a pulse of 3ω light at 35 J/cm^2 showing various traverses taken for microprobe analyses. All other laser parameters are: $1/e^2 = 0.98$ mm, pulse length (FWHM) = 7.5 ns and repetition rate = 10 Hz. (b) Si/O ratio determined for a fused silica standard (undamaged). (c) Si/O ratio determined along traverse E shown in (a). The distance is measured relative to the sample edge adjacent to the Si marker shown in (a).

To establish the reproducibility of the Si/O ratio measurements, a fused silica standard was analyzed 40 times over several days. The results are shown in Fig. 18(b). The Si and O concentrations at each point are reported as element weight percent (wt%) and the corresponding Si/O atomic ratio is also given. The analyses of the fused silica standard indicate a reproducibility in the Si/O ratio of 0.0033 at the 95% confidence level. None of the 40 anal-

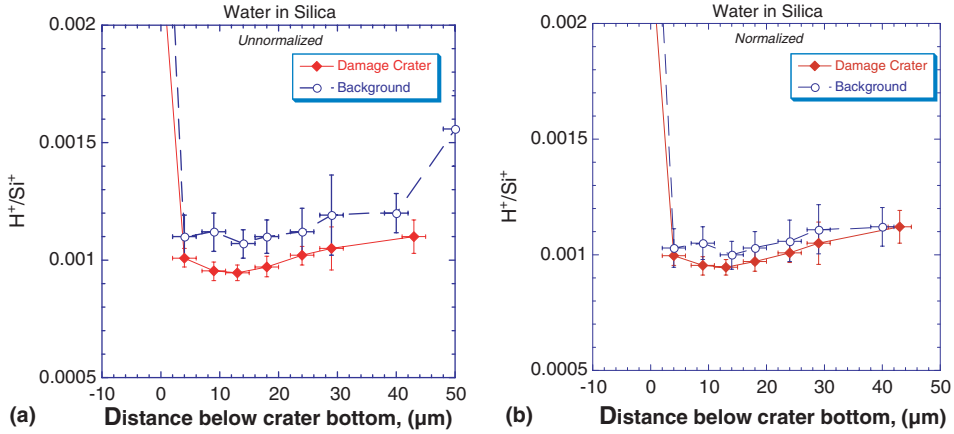

Fig. 19. SIMS depth profile plotted as H^+/Si^+ ratio vs distance immediately below the damage crater shown in Fig. 18(a) compared with undamaged area in the same fused silica optic: (a) un-normalized and (b) normalized. The distance is measured relative to the sample edge adjacent to the Si marker shown in Fig. 18(a). In each panel, the lines are drawn through the data points to serve as a guide to the eyes.

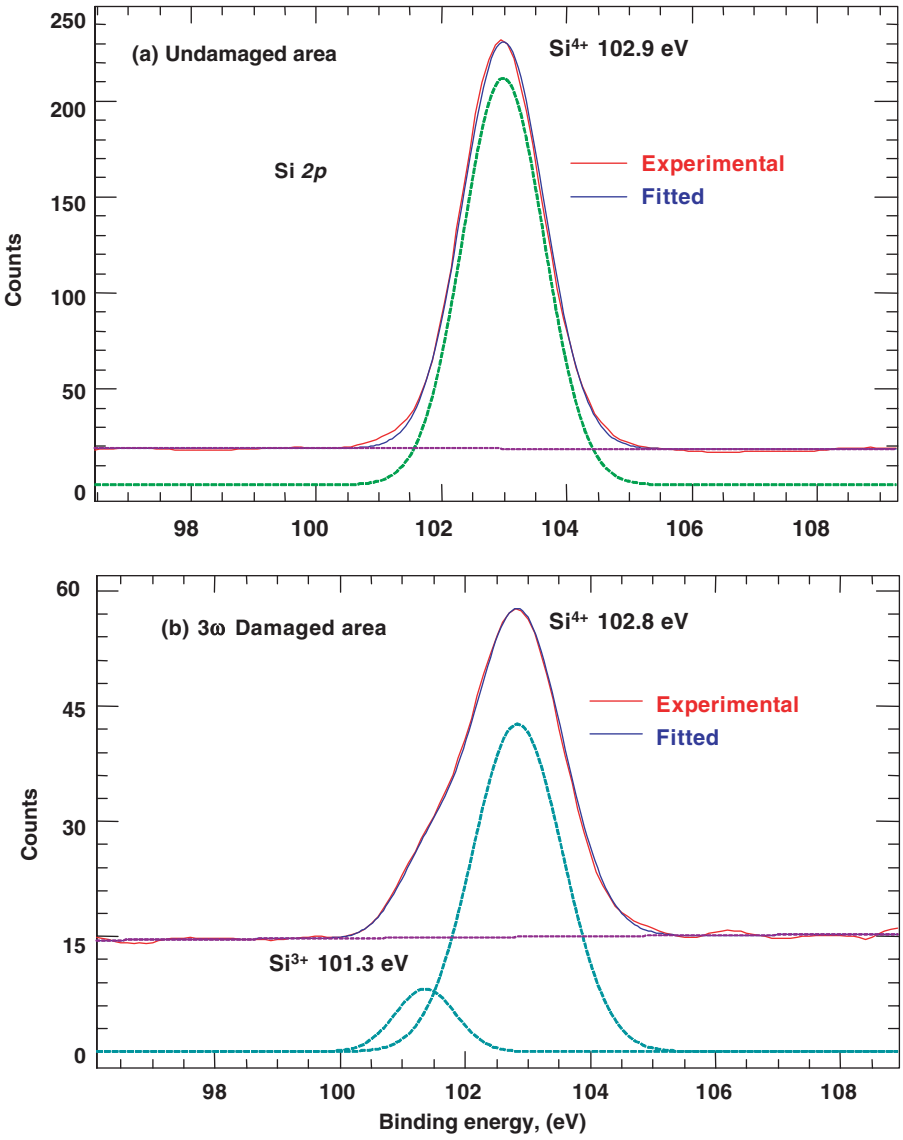

Fig. 20. Line profile of the Si 2p photoemission peak from (a) undamaged and (b) damaged fused silica induced by one pulse of 3ω light at 35 J/cm^2. The peak at 101.3 eV in (b) is indicative of existence of a Si^{3+} species [27] in the damaged region.

yses of this standard yield an Si/O ratio differing by more than 0.7% (relative) from the mean value of 0.4968 ± 0.0033, Fig. 18(b).

Fused silica is known [26] to be susceptible to damage created by the incident electron beam. Whenever the spacing between analysis points is 2 μm or less, the measured concentrations of Si and O exhibit anti-correlated variations, with O increasing and Si decreasing, in response to electron beam induced subsurface charging and localized heating of the material. Five of the seven traverses, including the two away from the crater, show essentially indistinguishable behavior of the Si/O ratio as a function of distance. For distances greater than ~40 μm, where the spacing between analyses is at least 5 μm, the Si/O ratio is constant at a value of 0.5 (±0.005). At distances between 40 and 10 μm the Si/O ratio is systematically lower in all traverses, with values between 0.485 and 0.493. Within 10 microns of the edge the Si/O decreases significantly and yields values between 0.473 and 0.487. The distance is reported in micrometers with 0 representing the bottom surface of the crater, i.e., the distance increases with depth below the crater.

To ameliorate the changes in Si/O related to beam damage, as deployed in traverse E, a 0.1 μm diameter electron beam was scanned in a line 20 μm long, oriented parallel to the top surface of the sample. Each 'point' in traverse E thus represents the Si and O concentration at a specific distance averaged over a ±10 μm wide swath, centered on the midline of the traverse. This protocol was very effective at alleviating the effects of beam damage while maintaining high precision, Fig. 18(c). For this traverse, a Si/O ratio of 0.497 ± 0.002 was determined. It is concluded therefore that within experimental accuracy of the microprobe analysis, the Si/O ratio at the bottom of the damage crater to a

depth of 100 μm was invariant with that of an undamaged fused silica standard.

4.2.2. Water content

Corning 7980 fused silica contains 800–1000 ppm of 'water' [11]. SIMS depth profiling was employed to investigate the H content (loss) in the vicinity of the damage site. The same microprobe sample was used for this study. SIMS analyses for H content along four traverses, three outside the damage crater and one through the center of the damage crater were performed. The data are presented as the $^{1}H^{+}/^{30}Si^{+}$ secondary ion ratio measured at each position along the four traverses. The distance is measured relative to the sample edge adjacent to the Si marker. Traverses 1, 2 and 4 correspond to undamaged regions, while traverse 3 runs through the center of the damage crater. The three traverses in undamaged regions yield similar results; the $^{1}H^{+}/^{30}Si^{+}$ ratio remains constant along each traverse to within 4 μm of the surface with an average value of 0.0014 ± 0.0002.

To calculate the best representative value for the H/Si ratio in the undamaged silica, the data for the three traverses in the undamaged regions were averaged. These data are shown in Fig. 19(a) together with the data for traverse through the crater. The uncertainties for the 'background' points are one standard deviation of the mean based on these three traverses. The data in Fig. 19(a) show a significant offset between the damaged and undamaged regions, which is most pronounced at distances between 10 and 24 μm. This suggests that the H/Si ratio is systematically lower in the damaged region of the silica.

However, the $^{1}H^{+}/^{30}Si^{+}$ secondary ion ratio is known to decrease with increased residence time of the sample under high vacuum. Since the first background traverse was initiated ~8 h before traverse #3, through the damaged region, and the last background traverse was not completed until ~8 h after traverse #3, we renormalized the data for the undamaged regions to correct for any instrumental bias. The renormalization factor was calculated using the offset between the background value of the $^{1}H^{+}/^{30}Si^{+}$ ion ratio at a distance of 40 μm and the value in the damaged region at a distance of 43 μm (0.936). The normalized data, shown in Fig. 19(b), still indicate a systematic difference in the $^{1}H^{+}/^{30}Si^{+}$ ion ratio between damaged and undamaged regions, although the difference is smaller than suggested by the un-normalized data. It is concluded therefore, that the silica immediately below the crater has a discernable lower water content than undamaged material as a result of water loss occurring during the crater-forming event.

4.2.3. Lower valence Si^{3+} species

Si 2p photoemission spectra were measured on sputter cleaned silica surfaces in both damaged and control (undamaged) areas. The latter was about ~4 mm away from the center of the damage crater. Systematic and careful analyses show that for the damage craters there is a substantial reduction in the integrated intensity and ~8% broadening (FWHM) of the Si 2p photoemission peak when compared with those of the corresponding control area. The Si 2p spectra for a damage site created with one pulse of 3ω light at 35 J/cm^2 and the associated control area are shown in Fig. 20. Each spectrum was fitted to a model function consisting of a linear background and Gaussian(s), and convoluted with the experimentally determined resolution function by using a standard χ^2 minimization procedure. As seen in Fig. 20(a), the undamaged area composes of a single Si 2p peak at a binding energy of 102.9 eV characteristic of Si^{4+}, whereas the damage crater consists of an additional Gaussian at a lower binding energy of 101.3 eV characteristic of the Si^{3+} species in Si–O films [27].

4.3. Point defects and their spatial distribution

It is well documented that a host of point defects can be generated in the fused silica structure upon irradiation with energetic particles such as neutrons, ions and electrons, and high energy electromagnetic radiations such as hard X-rays and gamma rays [28]. These defects may be electronic in nature involving a re-distribution of the local electron density to give rise to paramagnetic as well as diamagnetic centers, or structural in nature involving local atomic displacements from the normal random network glass structure. The latter defects may be oxygen-deficient or oxygen-excess. These radiation induced defects have been extensively studied and characterized over the last few decades using a variety of spectroscopic probes [29].

More recently, the point defects and their spatial distribution in fused silica induced by high fluence 3ω laser irradiation have been studied and characterized by Stevens-Kalceff et al. [30]. Using a combination of cathodoluminescence (CL) micro-spectroscopy and high sensitive ESR spectroscopy, six defects have been identified. These are: a non-bridging oxygen hole center (NBOHC), an oxygen deficient center (ODC(II)), a self

Table 3
Summary of observed 3ω laser-induced defects in fused silica: their optical and ESR properties (reproduced with permission of authors of Ref. [30])

Defect	Structure	Optical spectra (eV)	ESR
NBOHC	≡Si–O •	Abs: 2.0, 4.8 CL, PL: 1.9	$g_c = 2.0095$
STE	*	Abs: 4.6, 5.7 CL, PL: 2.3	
ODC	≡Si:···(Si≡) →|~4.4 Å|←	Abs: 3.15, 5.0, 6.9 CL, PL: 2.7, 4.4	Diamagnetic
O_2	O–O	Abs: 0.978 CL, PL: 0.97	
E'_γ	≡Si•···$^{+}$(Si≡)	Abs: 5.85 No. CL and PL obs.	$g_c = 2.00053$
E'_{74}	=HSi•···$^{+}$(Si≡)	No. CL and PL obs.	$g_c = 2.00125$

Notes: ≡ denotes Si bonding to 3 bridging oxygens in the silica glass structure; • = an unpaired electron; Abs. = absorption; CL = cathodoluminescence; PL = photoluminescence; * models for STE are known, but we do not know which type dominates here.

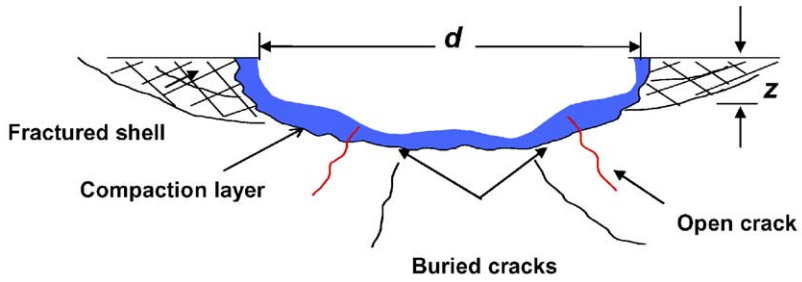

Morphology:
- crater diameter: 1 to ~100 μm, dependent on fluence, # of pulses, surface type
- z/d aspect ratio ~ 0.23 ± 0.05
- molten silica core surrounded by a near-concentric fractured shell
- surface depression ~20 nm

Cracks:
- macro, micro and nano in size
- open and buried
- cracks may be a key defect structure responsible for damage growth

Compaction Layer (~20% denser)
- on crater floor and wall, ~10 μm thick
- amorphous, no crystalline nano-particles
- shock compressed at ~ 20 GPa (max)
- high concentration of ODC and highly strained region
- H depleted w.r.t. to the silica bulk

Point defects:
- NBOHC, localized in fractured shell
- ODC, localized in molten core
- STE
- Interstitial O_2, low concentration, but detectable at the crater periphery
- E'γ : 5.0 x 10^{11} defects/ pulse at 30 J/cm^2
- E'_{74}: 2.2 x 10^{11} defects/ pulse at 30 J/cm^2

Fig. 21. Schematics of damage crater model, morphology, microstructure and point defects induced in fused silica by 3ω laser pulses at high fluences of 10–45 J/cm^2. All other laser parameters are take to be: $1/e^2 = 0.98$ mm, pulse length (FWHM) = 7.5 ns and repetition rate = 10 Hz.

trapped exciton (STE), a interstitial molecular oxygen center (O_2), the E'_γ and E'_{74}, centers. The latter two were detected using ESR spectroscopy and the former four with CL. The concentration of the E'_γ defect was determined to be $5.0 \pm 0.5 \times 10^{11}$/pulse at 30 J/cm^2 and that for the E'_{74} was $\sim 2.2 \times 10^{11}$/pulse at 30 J/cm^2. For completeness, a summary of the 3ω laser-induced defects in fused silica is reproduced in Table 3.

Using monochromatic imaging with the respective CL emission energies of 1.9 eV for NBOHC and 2.7 eV for ODC, the spatial distribution of the NBOHC and ODC(II) defects about the damage crater has been determined [31]. It was found that the NBOHC defect is rather delocalized around the damage crater in the fractured annulus, whereas the ODC(II) defect is spatially concentrated at the center of damage pit associated with the molten nodules shown in the SEM micrograph in Fig. 4(b). By varying the energy of the electron beam in the CL microscope, different penetration depths in the fused silica may be tuned and depth profiling of these defects has been obtained. Quantitative analysis shows that the maximum concentration of defects resulting from the laser-induced damage was found at the surface, consistent with damage initiation at the surface. The concentration of laser damage induced defects continuously decreases within the specimen, extending to a maximum depth of ~10 μm. The majority of the laser damage induced defects are found within the first ~5 μm [31].

4.4. Proposed model for 3ω damage crater in fused silica – the high fluence case

The above multi-length scale morphological and microstructural results lend credence to a recent phenomenological model for 3ω laser damage initiation craters in fused silica proposed by Feit et al. [18]. The model postulates the absorption of laser energy at a subsurface nano-particle in the glass and 'instantaneous' energy release due to a possible thermal explosion. Three regions of interest may be discernible. (i) An inner region in which material is subject to high pressure (shock wave from the micro-explosion) and high temperature to yield a resultant molten morphology, which was observed experimentally (Figs. 4 and 5). This resultant region suffers a H loss, undergoes densification (Figs. 13 and 14) and houses a concentration of oxygen deficient center [30] to yield a Si^{3+} signal in the XPS

spectrum (Fig. 20). (ii) A second region, annular to the first, has spalled material due to the shock wave reflected off the free surface. This region has a fractured morphology (Fig. 4(b)–(d)). (iii) An outermost region with high plastic deformation causing material cracking but no ejection (Fig. 12(a)).

The tomographic identification of a compaction layer at the bottom and wall of the damage crater (Fig. 15) substantiates the occurrence of a thermal explosion process which generates the shock wave needed for the compaction process. The current work also renders a quantitative validation for the (unusually) high compaction ($20\%^{+}$) in fused silica as predicted earlier by Woodcock et al. [32]. in their pioneering molecular dynamics (MD) study of silica glass. More recently, Kubota et al. [33] conducted a large-scale MD simulation (240 000 atoms) and reported a thickness of 300 Å for the compaction layer in fused silica for a shock pulse of 10 ps. Linear scaling of the simulated compaction layer with the duration of the shock to 7.5 ns yields 22.5 μm which is a factor of $\sim 2\times$ larger than the current XMT value of 10 μm. The damage crater may be schematically represented in Fig. 21 by its morphology, microstructure, cracks, compaction layer, point defects and local chemistry.

5. Conclusion

In summary, a suite of microscopic and spectroscopic techniques has been employed to characterize and elucidate quantitatively the morphology, densification and defects in fused silica induced by high fluence 3ω (355 nm) laser pulses. The high fluence structural data serve as an experimental baseline to explore the damage morphology and modified chemistry in NIF (National Ignition Facility) optics at the relevant fluences of 10–12 J/cm^2 at 3 ns pulse width. Furthermore, knowledge of the high fluence induced microstructure and defects may serve a dual function as (i) clues to understanding the laser-material interaction processes leading to damage and (ii) test for various viable mitigation processes for damage growth in NIF optics.

Acknowledgements

The work was performed under the auspices of the US Department of Energy by University of California, Lawrence Livermore National Laboratory under contract No. W-7405-Eng-48. We are thankful to C. Battersby and S. Miracle for preparation of the 3ω irradiated fused silica specimens used in this study. Technical assistance by E. Fearon, M. Kellam and M. Wall, and discussions with M.A. Stevens-Kalceff, A. Stesmans, M.D. Feit, A.M. Rubenchik, M.R. Kozlowski, Z.-L. Wu, L. Sheehan, M. Runkel, F.Y. Genin, A. Nelson, S. Demos, J.P. Plitzko and D. Milam are greatly appreciated. JW is also grateful to P.A. Baisden for suggestion and support of this work.

References

[1] E.M. Campbell, Fusion Technol. 26 (1994) 755.
[2] C. Seifa, D. Malakoff, Science 289 (2000) 1126.
[3] M.R. Kozlowski, R. Mouser, S. Maricle, P. Wegner, T. Weiland, SPIE 3578 (1999) 436.
[4] H. Hosono, K. Kawamura, in: G. Pacchioni, L. Skuja, D.L. Griscom (Eds.), Defects in SiO_2 and Related Dielectrics: Science and Technology, Kluwer Academic, Boston, 2000, p. 213.
[5] A.H. Guenther (Ed.), Laser-Induced Damage in Optical Materials, 25 Year Index, SPIE 2162 (1994).
[6] H. Hosono, M. Mizuguchi, H. Kawazoe, T. Ogawa, Appl. Phys. Lett. 74 (1999) 2755.
[7] K. Kajihara, Y. Ikuta, M. Hirano, H. Hosono, Appl. Phys. Lett. 81 (2002) 3164.
[8] A. Salleo, F.Y. Genin, J. Yoshiyama, C.J. Stolz, M.R. Kozlowski, SPIE 3244 (1998) 341;
A. Salleo, F.Y. Genin, J. Yoshiyama, C.J. Stolz, M.R. Kozlowski, SPIE 3578 (1999) 456.
[9] S.G. Demos, M.R. Kozlowski, SPIE 3933 (2000) 106;
S.G. Demos, M.R. Kozlowski, SPIE 4102 (2000) 316.
[10] N.L. Boling, M.D. Crisp, G. Dube, Appl. Optics 12 (4) (1973) 650.
[11] See hpfs@Corning.com, for Corning 7980 specification, 1999.
[12] L. Sheenan et al., SPIE 3578 (1998) 302.
[13] V. Karpenko et al., Rev. Sci. Instrum. 60 (1989) 451.
[14] J.H. Kinney et al., Nucl. Instrum. Meth. 347 (1994) 480.
[15] L.M. Cook, J. Non-Cryst. Solids 120 (1990) 152.
[16] J.R. Smith, S.D. Connell, J.A. Swift, J. Microcs. 196 (1999) 347.
[17] For a high resolution color stereo-SEM micrograph of this crater, email request to wong10@llnl.gov or exafs_materials@sbcglobal.net.
[18] M. Feit, L.W. Hrubesh, A.M. Rubenchik, Joe Wong, SPIE 4327 (2001) 316.
[19] M.D. Nordyke, J. Geophys. Res. 67 (1962) 1967.
[20] H. Melosh, Icarus 59 (1984) 234.
[21] Joe Wong et al., Appl. Phys. Lett. 48 (1986) 65.
[22] M. Catalano et al., J. Mater. Res. 8 (1993) 2893.
[23] B.R. Lawn, M.V. Swain, J. Mater. Sci. 10 (1975) 113.
[24] S.P. Marsh (Ed.), LASL Shock Hugoniot Data, University of California Press, Berkeley, 1980, p. 321.
[25] H. Sugiura, K. Kondo, A. Sawaoka, J. Appl. Phys. 52 (1981) 3375;
H. Sugiura, K. Kondo, A. Sawaoka, J. Appl. Phys. 81 (1997) 1651.
[26] M.A. Stevens-Kalceff, Phys. Rev. Lett. 84 (2000) 3137.
[27] F.J. Himpsel, F.R. McFeely, A. Taleb-Ibrahimi, J.A. Yarmoff, Phys. Rev. B 38 (1988) 6084.
[28] Joe Wong, C.A. Angell, Glass: Structure by Spectroscopy, Marcel Dekker, New York, 1976.
[29] L. Skuja, J. Non-Cryst. Solids 239 (1998) 16.
[30] M.A. Stevens-Kalceff, A. Stesmans, Joe Wong, Appl. Phys. Lett. 80 (2002) 758.
[31] M.A. Stevens-Kalceff, Joe Wong, J. Appl. Phys. 97 (2005) 113519.
[32] L.V. Woodcock, C.A. Angell, P. Cheeseman, J. Chem. Phys. 65 (1976) 1565.
[33] A. Kubota, M.-J. Caturla, J.S. Stolken, M.D. Feit, Opt. Exp. 8 (2001) 611.